



Article

Selective Chemical Vapor Deposition Growth of WS₂/MoS₂ Vertical and Lateral Heterostructures on Gold Foils

Zixuan Wang^{1,2}, Wenshuo Xu^{2,3,*}, Benxuan Li^{2,4}, Qiaoyan Hao², Di Wu², Dianyu Qi², Haibo Gan², Junpeng Xie¹, Guo Hong^{1,5,*} and Wenjing Zhang^{2,*}

- ¹ Institute of Applied Physics and Materials Engineering, University of Macau, Avenida da Universidade, Taipa 999078, Macau; yb87822@umac.mo (Z.W.); jepsenxie@foxmail.com (J.X.)
- ² International Collaborative Laboratory of 2D Materials for Optoelectronics Science and Technology of Ministry of Education, Institute of Microscale Optoelectronics, Shenzhen University, Shenzhen 518060, China; bl398@cam.ac.uk (B.L.); hqy@szu.edu.cn (Q.H.); physicswudi@163.com (D.W.); qidianyuyi@sina.com (D.Q.); ganhaibo@szu.edu.cn (H.G.)
- ³ Department of Physics, National University of Singapore, 2 Science Drive 3, Singapore 117551, Singapore
- ⁴ Electrical Engineering Division, Engineering Department, University of Cambridge, 9 JJ Thomson Avenue, Cambridge CB3 0FA, UK
- ⁵ Department of Physics and Chemistry, Faculty of Science and Technology, University of Macau, Avenida da Universidade, Taipa 999078, Macau
- * Correspondence: wensxu@nus.edu.sg (W.X.); ghong@um.edu.mo (G.H.); wjzhang@szu.edu.cn (W.Z.)

Abstract: Vertical and lateral heterostructures consisting of atomically layered two-dimensional (2D) materials exhibit intriguing properties, such as efficient charge/energy transfer, high photoresponsivity, and enhanced photocatalytic activities. However, the controlled fabrication of vertical or lateral heterojunctions on metal substrates remains challenging. Herein, we report a facile and controllable method for selective growth of WS₂/MoS₂ vertical or lateral heterojunctions on polycrystalline gold (Au) foil by tuning the gas flow rate of hydrogen (H₂). We find that lateral growth is favored without H₂, whereas vertical growth mode can be switched on by introducing 8–10 sccm H₂. In addition, the areal coverage of the WS₂/MoS₂ vertical heterostructures is tunable in the range of 12–25%. Transmission electron microscopy (TEM) and selected area electron diffraction (SAED) results demonstrate the quality and absence of cross-contamination of the as-grown heterostructures. Furthermore, we investigate the effects of the H₂ flow rate on the morphology of the heterostructures. These pave the way to develop unprecedented 2D heterostructures towards applications in (opto)electronic devices.

Keywords: chemical vapor deposition; 2D materials; heterostructures; selective growth



Citation: Wang, Z.; Xu, W.; Li, B.; Hao, Q.; Wu, D.; Qi, D.; Gan, H.; Xie, J.; Hong, G.; Zhang, W. Selective Chemical Vapor Deposition Growth of WS₂/MoS₂ Vertical and Lateral Heterostructures on Gold Foils. *Nanomaterials* **2022**, *12*, 1696. <https://doi.org/10.3390/nano12101696>

Academic Editor: Antonio Di Bartolomeo

Received: 16 April 2022

Accepted: 13 May 2022

Published: 16 May 2022

Publisher's Note: MDPI stays neutral with regard to jurisdictional claims in published maps and institutional affiliations.



Copyright: © 2022 by the authors. Licensee MDPI, Basel, Switzerland. This article is an open access article distributed under the terms and conditions of the Creative Commons Attribution (CC BY) license (<https://creativecommons.org/licenses/by/4.0/>).

1. Introduction

Two-dimensional (2D) materials, including graphene, hexagonal boron nitride (h-BN), and transition metal dichalcogenides (TMDs) [1–4], play a crucial role in advanced devices due to their unique properties [5–8]. 2D heterostructures consisting of different atomically thin components are formed either through layer-by-layer stacking or in-plane stitching [9–11]. The synthetic techniques of transition metal dichalcogenides (TMDs)-based vertical and lateral heterostructures (VHs and LHs) have been studied in recent years, among which chemical vapor deposition (CVD) stands out as a controllable and scalable method. Gong et al. utilized CVD to achieve the selective growth of WS₂/MoS₂ VHs and LHs on SiO₂/Si substrate by varying the temperatures [12]. The mediating role of the growth temperature was further verified by the epitaxial growth of WS₂/MoS₂ VHs with reverse stacking sequences on sapphire [13]. In addition to changing the temperature, Zhu et al. controlled the growth of WS₂/MoS₂ VHs and LHs by introducing hydroxide molecules after the growth of the bottom layer MoS₂. This can lead to the formation of –OH groups on the surface of the MoS₂ at low temperature, thereby hindering the nucleation of the top layer WS₂ and resulting in WS₂/MoS₂ LHs. The decomposition of

the $-OH$ at high temperature allows the preferential growth of WS_2 on top of MoS_2 and creation of WS_2/MoS_2 VHs [14]. The involvement of hydroxides may cause contamination and deteriorate the intrinsic properties of the TMD constituents. Zhang et al. used an additional substrate to confine the growth area of MoS_2/WS_2 VHs, and decreased the nucleation density of the top layer WS_2 on the bottom layer MoS_2 by introducing H_2 as an additional carrier gas [15]. Furthermore, Au foils are considered strongly interactive and concurrently compatible with the growth of 2D materials. Both theoretical analysis and experimental observations show that most TMD possess three-fold symmetry and present very similar epitaxial behavior on substrates [13,16,17]. However, the selective fabrication of 2D TMDs-based VHs and LHs on metal substrates has not been investigated, which is important for lowering the contact resistance between the TMD semiconductor channel and the metal electrodes.

In this work, we report the selective growth of WS_2/MoS_2 VHs and LHs on polycrystalline Au foil by tuning the gas flow rate of hydrogen. The synthesis approach is facile and the switching of growth mode is achieved via monocontrol. WS_2/MoS_2 LHs are preferentially formed without H_2 , whereas H_2 is necessary for the growth of WS_2/MoS_2 VHs. Moreover, we study the influence of the H_2 flow rate on the resultant domain morphology. The effect of substrates is also studied by comparing the growth results on Au, c-sapphire and SiO_2/Si . Our work will be helpful for the synthesis of unprecedented two-dimensional materials with outstanding properties.

2. Materials and Methods

2.1. Pre-Treatment of Polycrystalline Au Foils

First, commercially available Au foils (Alfa Aesar, Thermo Fisher Scientific, Ward Hill, MA, USA, 25 μm thickness, 99.985% metal basis, LOT: R23F014) were cut into an appropriate size. Then, small pieces of Au foils were ultrasonically cleaned by an acetone solution and IPA solution for 10 min, respectively. After that, the cleaned Au foils were annealed in the CVD at 1000 $^{\circ}C$ for 3 h to release the stress and expose the grain boundaries, and Ar with a flow rate of 100 sccm was introduced during the whole annealing process.

2.2. CVD Growth Process of LHs and VHs

A chemical vapor deposition device with only one heating zone was shown in Figure 1a. Three boats (named boat 1, boat 2 and boat 3) were placed in quartz tubes from upstream to downstream. Boat 2 with WO_3 was put in the center of the heating zone, and the Au foil was also placed in boat 2 close to WO_3 with a distance of about 0.5 cm. Boat 1 with MoO_3 was put in the left of the heating zone, while boat 3 with S powder was put outside the heating zone in the right. In addition, both boat 1 and boat 3 have one magnet in them to ensure they can be moved during the growth process. The chemical vapor deposition process can be divided into three stages: growth stage I was for the first monolayer MoS_2 , and growth stage III was for the second monolayer WS_2 (relatively higher growth temperature), while transition stage II was between the two growth stages. Ar was used as the carrier and protective gas with a flow rate of 80 sccm during the whole process.

2.3. WS_2/MoS_2 LHs Growth on Au Foils

MoO_3 powder (99.9%, 2 mg) was put into boat 1, WO_3 powder (99.9%, 3 mg) and Au foil were put into boat 2, while sulfur powder (99.9%, 20 mg) was put into boat 3. In the beginning, WO_3 was placed at the center of the heating zone. MoO_3 was placed in the room temperature position in a quartz tube to reduce the vast evaporation, while S was placed downstream at the temperature of about 200–250 $^{\circ}C$. Then, the temperature of the heating zone was raised up from room temperature to 750 $^{\circ}C$ in 38 min and kept at 750 $^{\circ}C$ for 5 min for the growth of the first monolayer MoS_2 . The Mo source was sent to a 700 $^{\circ}C$ position in the heating zone (the exact location of 700 $^{\circ}C$ in the heating zone can be determined by a K type thermocouple thermometer when the heating center reaches 750 $^{\circ}C$) as soon as the programmed temperature reached 750 $^{\circ}C$, and the distance between Mo source and Au foil

was kept at 7.5 cm. Then, boat 1 was pulled out to room temperature to cut off the supply of Mo source after the growth stage I. Meanwhile, change the position of boat 3 to a suitable temperature zone to ensure the S stable supply. Next, the temperature of the heating zone was raised up to 850 °C in 4 min and maintained for 3 min for the growth of WS₂. Finally, the tube furnace was quickly cooled down to room temperature after the growth stage III. The temperature program for WS₂/MoS₂ LHs growth is shown in Figure 1c.

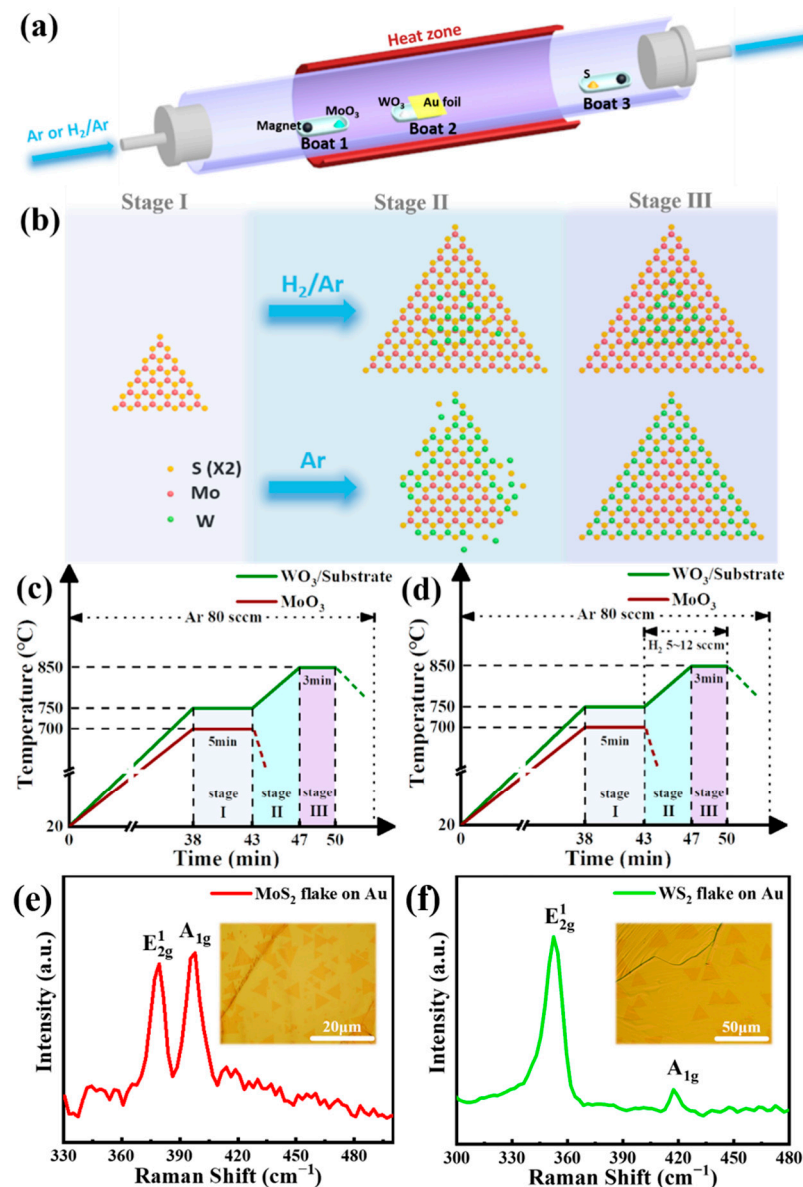


Figure 1. (a) Schematics of the CVD setup for the growth of WS₂/MoS₂ LHs and VHs; (b) schematic illustrations of WS₂/MoS₂ LHs and VHs growth process; (c,d) temperature program of the CVD growth process for WS₂/MoS₂ LHs and VHs, respectively; (e,f) Raman spectra of as-grown MoS₂ and WS₂ monolayers, respectively. Insets: Corresponding optical microscopic images of the MoS₂ and WS₂ flakes on Au foil.

2.4. WS₂/MoS₂ VHs Growth on Au Foils

Similar to the conditions described for WS₂/MoS₂ LHs growth above, H₂ with a flow rate of 5–12 sccm was introduced during the transition stage II and growth stage III. Keep other experimental parameters and conditions the same as those in WS₂/MoS₂ LHs growth. The temperature program for WS₂/MoS₂ VHs growth is shown in Figure 1d.

2.5. MoS₂ and WS₂ Monolayers Growth on SiO₂/Si and C-Sapphire Substrates

For MoS₂ monolayers growth, only reserve and extend growth stage I to 20 min; for WS₂ monolayers growth, only reserve and extend growth stage III for 20 min. Keep the other parameters and conditions the same as those in the growth case of WS₂/MoS₂ LHs.

2.6. Transfer Process

After growth, poly methyl methacrylate (PMMA) (10% wt., in anisole) was spin-coated following 2000 rpm for 90 s, and then the sample was baked at 180 °C for 5 min. The PMMA-sample-Au foil was put into the Au etchant solution (I₂ and KI in a mol ratio of 1:1, dissolved in 50 mL deionized water) at 50 °C for 3 h to remove Au foil. The floating film was transferred into DI water to remove the etchant ions and was finally lifted onto a cleaned SiO₂/Si substrate. The substrate was then dipped into acetone to remove the PMMA layer.

2.7. Characterization

OM images were obtained on an optical microscope (Leica DM2700M RL, Wetzlar, Germany). AFM characterization was performed on a Dimension ICON microscope from Bruker (365 Boston Rd. Billerica MA 01821, USA). Raman spectra, PL spectra, and mappings were collected via Raman spectroscopy (Alpha 300, WITec with 532 nm laser, Lise-Meitner-Str. 6 D-89081 Ulm, Germany). The composition and valence of elements were explored by using an XPS (ESCALab250Xi, 81 Wyman Street, Waltham, MA, 02454, USA), and TEM images and element distribution of the heterojunction were analyzed by EDS mapping on a TEM (JEM-3200FS, JEOL, Street No.6, Haidian District, Beijing 100190, China).

3. Results and Discussion

WS₂/MoS₂ LHs and VHs were fabricated via one-pot CVD. The schematic diagrams of the CVD setup for the growth of the heterostructures the growth process of the VHs are shown in Figure 1a,b, respectively. Distinct from the conventional placements of the precursors, we loaded sulfur powder at the downstream region. This positioning strategy only allows a very small flux of S to get involved in the growth stages by slow diffusion. Therefore, the MoO₃ is prevented from being exposed to a large amount of S, whereby decreasing the cross-contamination at the resultant heterointerface [18]. The temperature programs for growing the WS₂/MoS₂ LHs and VHs are shown in Figure 1c,d, respectively. The growth process can be divided into three stages: Stage I represents the growth of the bottom MoS₂ monolayer, and Stage III represents the growth of the top WS₂ monolayer at a higher temperature, and Stage II is a transition stage. Since the boiling point of WO₃ is higher than that of MoO₃, the WO₃ is placed closer to the Au substrate and remains at the same location during the growth. On the contrary, MoO₃ powder is transitioned from a room temperature region into the growth area (~700 °C) as soon as the growth program reaches Stage I, and returns to the room temperature region to cut off the Mo supply immediately after Stage I. More details of the synthesis are described in the Experimental Section. Typical Raman spectra from MoS₂ and WS₂ monolayer domains were shown in Figure 1e,f, respectively. The Raman peaks centered at 384.5 and 403.5 cm⁻¹ correspond to E_{2g}¹ and A_{1g} vibrational modes of MoS₂, while Raman peaks located at 419 cm⁻¹ and 355.5 cm⁻¹ correspond to E_{2g}¹ and A_{1g} vibrational modes of WS₂. E_{2g}¹ is an in-plane vibration mode, corresponding to the in-plane vibrations of Mo/W and S atoms, while A_{1g} is the out-of-plane vibration mode of the two S atoms along the z-axis of the TMD unit cell [5]. Additionally, the frequency differences (Δ) for MoS₂ and WS₂ were measured to be 19 and 63.5 cm⁻¹, respectively, confirming that the as-grown MoS₂ and WS₂ are both monolayer [19]. The insets present the optical microscopic images of the as-grown MoS₂ and WS₂ single crystals on Au foils. The lateral sizes of the MoS₂ and WS₂ domains are as large as ~10 and ~15 μm, respectively. The growths of the MoS₂ and WS₂ domains with similar sizes on SiO₂/Si and c-sapphire substrates (Figure S1) are much slower (20 min) than those on Au foils (5 min), indicating that Au plays a catalytic role in the synthesis.

Given that the laser exciton would lead to energy transfer from the MX_2 to the Au, the as-grown WS_2/MoS_2 LHs and VHs were transferred onto SiO_2/Si substrates to further characterize the WS_2/MoS_2 heterostructures. The schematic illustration of the transfer process was presented in Figure S2, and the details of the transfer method described in the Materials and Methods section.

Following the growth process in Figure 1f, the WS_2/MoS_2 LHs consisting of a MoS_2 monolayer inside and a WS_2 monolayer outside were produced. Figure 2a shows the optical image of as-transferred WS_2/MoS_2 LH on the SiO_2/Si substrate. The edge length of the inner MoS_2 monolayer is about $10\ \mu\text{m}$. Raman mapping for the area is labeled by a brown dotted square, and the intensity mappings for the Raman characteristic peaks of MoS_2 ($383\ \text{cm}^{-1}$) and WS_2 ($355\ \text{cm}^{-1}$) are shown in Figure 2b–d, respectively. To measure the thickness of the as-prepared WS_2/MoS_2 LH, AFM was carried out. Figure 2e shows the AFM surface morphology and the corresponding height profiles across the whole WS_2/MoS_2 LH. The thickness of the sample is about $0.8\ \text{nm}$, thereby proving the monolayer characteristics of the as-synthesized WS_2/MoS_2 LH [20]. Additionally, Raman and PL spectroscopy were used to characterize the LH structure. Raman single spectra acquired from the red point shows only the E_{2g}^1 (at $383\ \text{cm}^{-1}$) and A_{1g} (at $402\ \text{cm}^{-1}$) peaks of the MoS_2 , and the spectra collected from the green point show only the E_{2g}^1 (at $355\ \text{cm}^{-1}$) and A_{1g} (at $418\ \text{cm}^{-1}$) peaks of the WS_2 (Figure 2f). The difference between the two modes is about $19\ \text{cm}^{-1}$ and $63\ \text{cm}^{-1}$, respectively, indicating that inside MoS_2 and outside WS_2 are both monolayers [12]. On the other hand, the PL spectra collected from the red point show a strong peak and a weak peak at $678\ \text{nm}$ and $620\ \text{nm}$, respectively (Figure 2g). The peak at $678\ \text{nm}$ is related to the direct transition in the MoS_2 monolayer [5], proving that the triangular area inside is a MoS_2 monolayer, and the peak at $620\ \text{nm}$ is attributed to the B-exciton because of the energy level splitting [21]. In contrast, the PL spectra collected from the green point show a strong peak only at a wavelength of $638\ \text{nm}$, corresponding to the $1.96\ \text{eV}$ direct excitonic transition energy in the monolayer WS_2 outside. These results confirm the formation of an in-plane WS_2/MoS_2 heterostructure, with a triangular monolayer MoS_2 domain inside and WS_2 outside.

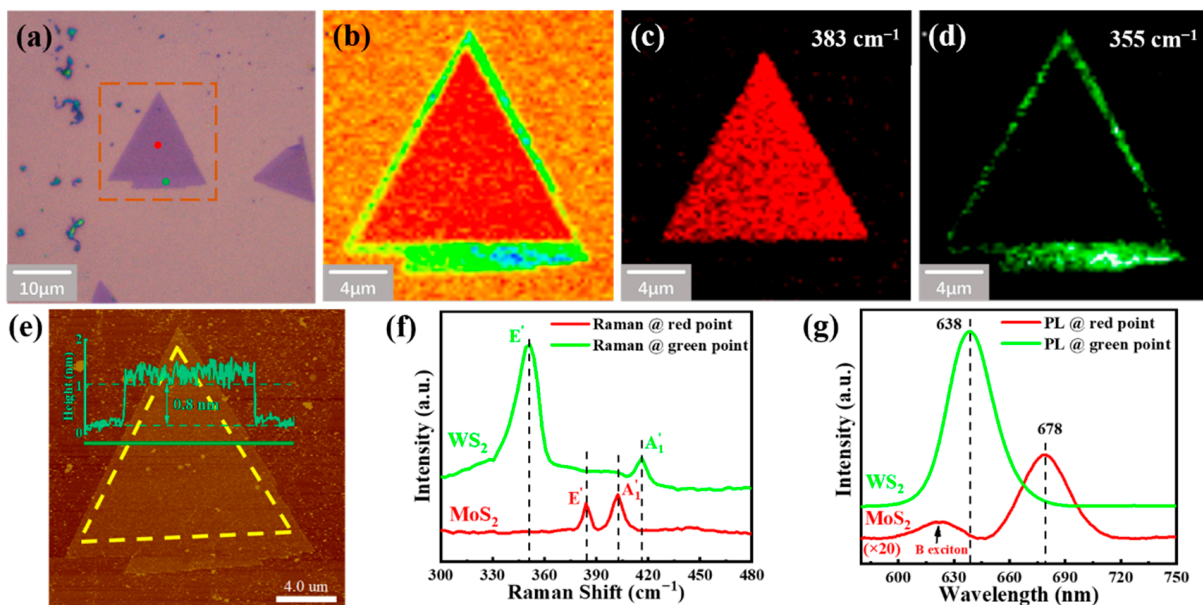


Figure 2. (a) Optical microscopic image of an as-grown WS_2/MoS_2 LH transferred from Au foil to SiO_2/Si substrate; (b) Raman intensity map; (c,d) Raman intensity maps at 383 and $355\ \text{cm}^{-1}$, respectively. The excitation wavelength is $532\ \text{nm}$; (e) AFM image of the WS_2/MoS_2 LH acquired from the boxed region in (a). Inset: corresponding height profile measured along the green line; (f) Raman spectra and (g) PL spectra collected at different positions of the WS_2/MoS_2 LH shown in (a).

XPS measurements were also conducted to demonstrate the elemental compositions, and the results are shown in Supporting Information. Figure S3a shows the optical microscopic image of the as-grown WS₂/MoS₂ LHs. Figure S3b presents the wide XPS scan collected from the heterojunction area, indicating the existence of Au, W, Mo, and S elements. As shown in Figure S3c–f, respectively, Au 4f (Figure S3c) exhibits two peaks at around 84.2 eV (Au 4f_{7/2}) and 88 eV (Au 4f_{5/2}), which shows the presence of Au (0). The two peaks at around 32.9 and 35.1 eV can be assigned to W 4f_{7/2} and W 4f_{5/2}, respectively, presenting W (+4) as shown in Figure S3d. There are two major peaks of the Mo element that appeared at around 232.3 (Mo 3d_{3/2}) and 229.5 eV (Mo 3d_{5/2}), respectively, as the presence of Mo (+4) (Figure S3e). Another peak at 226.8 eV corresponds to S 2s (labeled with the blue arrow). Figure S3f shows two peaks at around 163.6 and 162.2 eV, corresponding to S 2p_{1/2} and S 2p_{3/2}, respectively. All these XPS results are consistent with the values for WS₂/MoS₂ heterostructures reported previously [22].

WS₂/MoS₂ VH, consisting of a MoS₂ monolayer at the bottom and a WS₂ monolayer on the top, can be prepared on Au foil by introducing a suitable gas flow rate of hydrogen. Figure 3a shows the typical optical image of the as-transferred stacked WS₂/MoS₂ VH. It can be seen that the edge length of the bottom layer MoS₂ is ~10 μm, which is in line with those samples shown in Figures 1b and 2a. In addition, the optical contrast was much larger compared to the LH shown in Figure 2a. Raman intensity mapping was conducted for the region squared in Figure 3a. Notably, the outer vertical contact area in the Raman mappings exhibit a slight color difference, attributed to the large laser spot size (~1 μm) used in our experiment. Figure 3c,d shows the Raman intensity maps corresponding to the characteristic peak of MoS₂ at 383 cm⁻¹ and that of WS₂ at 355 cm⁻¹, respectively. The WS₂ domain in Figure 3d is fully overlapped with the MoS₂ domain in Figure 3c, indicating that the MoS₂ and WS₂ monolayers are vertically stacked rather than laterally stitched [12]. This is also verified by atomic force microscopy (AFM). Figure 3e shows the corresponding height profile acquired along the green section line, which demonstrates changes of thickness caused by different layers, corresponding to 0.75 and 0.72 nm, respectively. Furthermore, Raman and PL were used to characterize the vertical bilayer heterostructure, as shown in Figure 3f,g, respectively. The red line and green line correspond to the red point monolayer region and green point bilayer region labeled in Figure 3a. The Raman spectrum collected from the monolayer area (red point) shows only E_{2g}¹ (at 382 cm⁻¹) and A_{1g} (at 401.5 cm⁻¹) peaks of the MoS₂, confirming that the bottom layer is MoS₂. The Raman spectrum acquired from the bilayer area (green point) shows two additional peaks located at 355 and 418 cm⁻¹, which are related to the E_{2g}¹ mode and the A_{1g} modes of the upside WS₂ monolayer, respectively. Moreover, the differences between the two modes are 19.5 and 63 cm⁻¹, respectively, indicating that the bottom MoS₂ and top WS₂ are both monolayers. The PL spectra of MoS₂ (red curve in Figure 3g) acquired from the monolayer region (red point marked in Figure 3a) show a strong peak and a weak peak at a wavelength of 678 and 620 nm, corresponding to the A excitons and B excitons of the MoS₂ monolayer. However, at the bilayer region (green point labeled in Figure 3a), two prominent peaks were observed at wavelengths of 638 and 678 nm, attributed to the top WS₂ monolayer and bottom MoS₂ monolayer [13], respectively. However, the PL intensity from the heterostructure area is much weaker than that of the MoS₂ monolayer. Such PL quenching is attributed to the excitation-induced interlayer charge transfer across the type II heterojunction between MoS₂ and WS₂ [23]. As shown in Figure 3h, another PL peak with a lower intensity at 875 nm is observed in the VHs (green point marked in Figure 3a), which could originate from the interlayer excitonic transition between the minimum conduction band of MoS₂ and the maximum valence band of WS₂. This demonstrates the strong interlayer interactions of the WS₂/MoS₂ VHs.

Our results indicate that introducing H₂ or not exhibiting such a positive effect of selectively growing WS₂/MoS₂ VHs or LHs on Au foil during the transition stage II and the growth stage III. The reason could be explained as follows: on the one hand, H₂ can etch away excess nucleation points on the bottom layer, and the W source can reach the surface of the first as-grown MoS₂ monolayer during the growth stage III. Thus, uncontrolled

homogeneous nucleation and multi-nucleation can be prevented effectively. On the other hand, proper H₂ gas flow could saturate the dangling bonds on the edges of the as-grown MoS₂ monolayer and hinder the laterally epitaxial growth [18]. The chemical potential of the edges is considerably higher compared to that of the basal planes [22,24]. Consequently, the top WS₂ monolayer prefers to deposit on the as-grown monolayer surface rather than laterally grow in the H₂ atmosphere. Figure S4 shows the low-magnification optical microscopic image of the as-grown WS₂/MoS₂ LH and VH on Au foils.

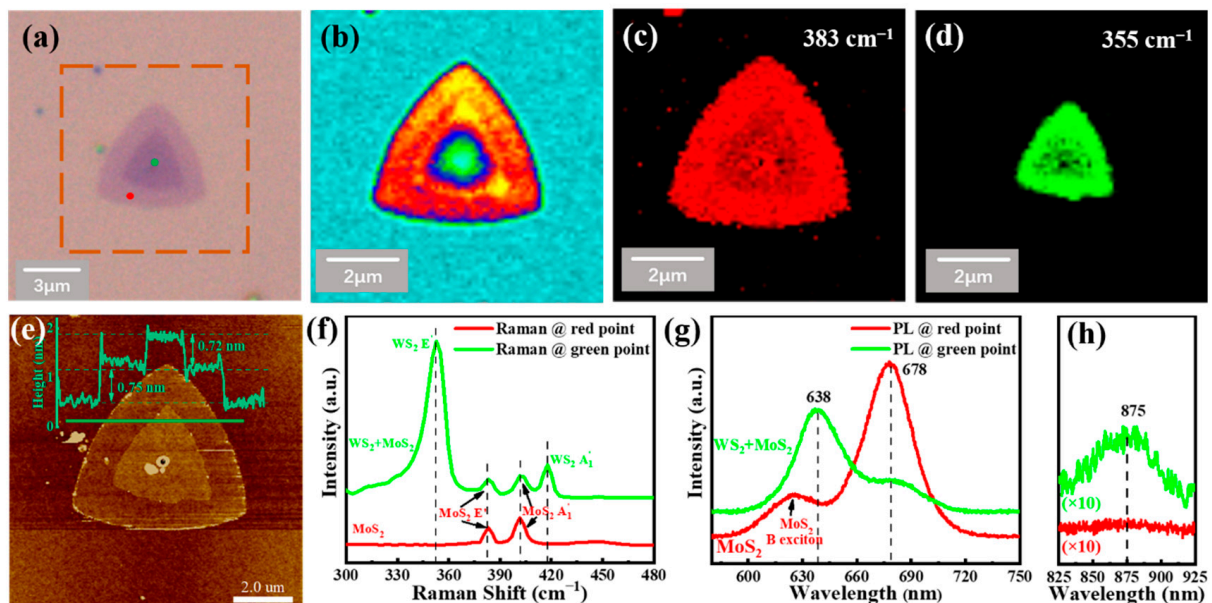


Figure 3. (a) Optical microscopic images of the as-grown vertical WS₂/MoS₂ heterostructure transfer from Au foil to SiO₂/Si; (b) Raman intensity map; (c,d) Raman intensity mapping at 383 cm⁻¹ (c), and at 355 cm⁻¹ (d), corresponding to the characterization peaks of MoS₂ and WS₂, respectively. The excitation laser is 532 nm; (e) AFM image of the as-grown vertical WS₂/MoS₂ heterostructures collected from the labeled area in figure (a). The inset was a corresponding height profile acquired along the gray section line. Raman single spectra (f) and PL single spectra (g) collected from different points of WS₂/MoS₂ LH sample, the red line and green line are corresponding to the red point and green point labeled in (a), respectively. (h) The PL spectra at a longer wavelength, and the curves were both magnified by ten times.

The structure of the WS₂/MoS₂ VHs was examined by transmission electron microscopy (TEM). The image contrast in Figure 4a indicates the boundary between the bilayer VH (bright area) and the monolayer MoS₂ (darker area). High-resolution TEM (HRTEM) was performed to further evaluate the qualities of as-grown WS₂/MoS₂ VHs, and results are presented in Figure 4c. Figure 4b is the corresponding energy dispersive X-ray spectroscopy (EDS) elemental maps of the region displayed in Figure 4a. All constituent components (Mo, W, and S) are homogeneously distributed over the whole scanning range. The negligible signals of W in the MoS₂ region excludes the cross-contamination during the CVD. The split spots in the corresponding selected area electron diffraction (SAED) pattern demonstrate the crystal structures of WS₂ and MoS₂, respectively, which are associated with the hexagonal symmetries of MoS₂ and WS₂ lattices.

Next, we investigate the effects of the H₂ flow rates on the morphology of the WS₂/MoS₂ heterostructures. Figure 4d–h shows the structural evolution with an increase in the H₂ flow rate. When no H₂ is introduced (gas flow rate = 0 sccm), only LHs are formed on the Au substrate, and no VHs are observed (Figure 4d). When the H₂ flow rate is increased to 5 sccm, small WS₂ monolayer domains (edge length ~1–2 μm) are grown on top of the monolayer MoS₂ (Figure 4e), suggesting that WS₂/MoS₂ VHs start to form under this condition. When the H₂ flow rate is increased to 8 sccm, the sizes of the top WS₂

monolayer domains are increased to $\sim 2\text{--}5\ \mu\text{m}$, with little change in the sizes of the bottom MoS_2 monolayer domains ($\sim 10\text{--}15\ \mu\text{m}$), and the edges of both MoS_2 and WS_2 domains are flat (Figure 4f). When the H_2 flow rate is increased to $\sim 10\ \text{sccm}$, as shown in Figure 4g, the sizes of top WS_2 monolayer domains are still $\sim 2\text{--}5\ \mu\text{m}$; however, the edges of the bottom MoS_2 monolayer domains start to display jagged features (see in Figure S5a,b), and the domain sizes are decreased to $\sim 5\text{--}10\ \mu\text{m}$. The formation of jagged edges indicates a change in the growth kinetics [25], which may stem from the etching effect of H_2 [26]. With the further increase in H_2 gas flow rate to $\sim 12\ \text{sccm}$, as shown in Figure 4h, the sizes of the top layer WS_2 domains are much smaller, and the bottom MoS_2 layers show irregular shapes, indicating that the H_2 induced etching dominated the growth of top and bottom layers.

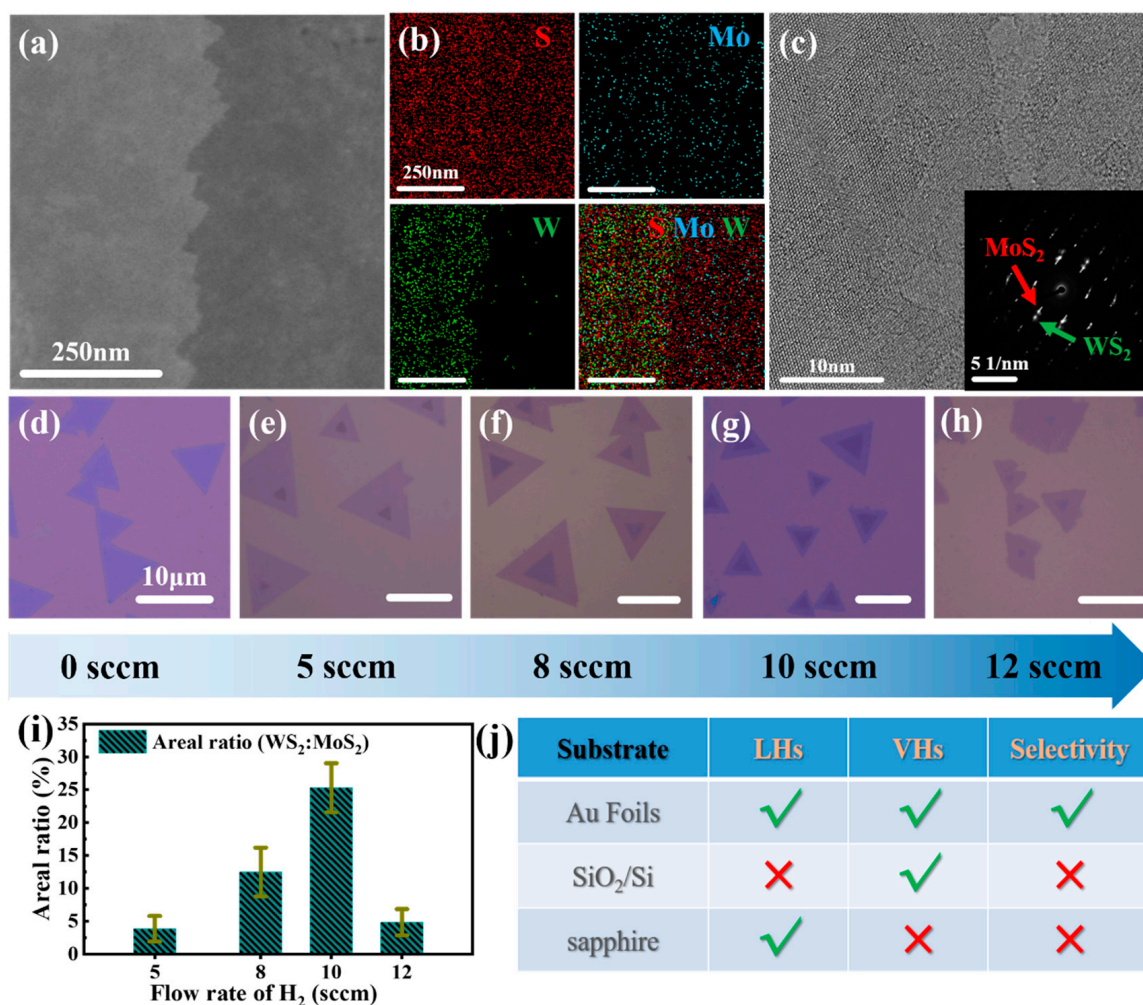


Figure 4. (a) TEM image of as-grown WS_2/MoS_2 VH; (b) the corresponding energy dispersive X-ray spectroscopy (EDS) elemental maps of the region displayed in (a); (c) HRTEM image of an as-grown WS_2/MoS_2 VH. The corresponding selected area electron diffraction (SAED) pattern is shown in the inset; (d–h) optical microscopic images reveal the morphology evolution of the as-transferred WS_2/MoS_2 heterostructures under a different gas flow rate of hydrogen; (i) bar chart of the $\text{WS}_2:\text{MoS}_2$ areal ratio calculated based on (d–h) under different H_2 flow rates; (j) selectivity table to summarize the synthesis of LHs/VHs in various substrates.

Furthermore, we calculated the areal ratios of $\text{WS}_2:\text{MoS}_2$ to evaluate the morphology evolution as the H_2 flow rate increases. The statistical results are displayed in Figure 4i. For comparison, the results of the WS_2/MoS_2 heterostructures grown on different substrates depending on whether or not hydrogen is supplied are presented in Figure S6. Stacked VHs are predominantly formed on SiO_2/Si substrate when there is a supply or absence of

H₂ (see in Figure S6a,b), while the growth of WS₂/MoS₂ LHs is favorable on the c-sapphire substrate whether H₂ is introduced or not (Figure S6c,d). Notably, it seems passing H₂ will change the morphology of heterostructure domains into irregular rather than triangle-shapes. However, we do not find LHs on SiO₂/Si or VHs on sapphire substrates by introducing H₂, which is quite different from the results collected from Au foils. The following AFM images (Figure S6e–h) and corresponding profiles (Figure S6i–l) further support the conclusions mentioned above. The different results on metal substrate (Au) and insulating substrate (sapphire and SiO₂/Si) can be ascribed to the TMD-substrate interactions [17]. Hence, we find it viable to dictate the growth direction (lateral or vertical) by tailoring the relationship between the adlayer material and the substrate. Finally, these substrates are classified in the selectivity table (Figure 4j) according to the synthesis results in our experimental system and the summing-up is further proof that the Au foils have selective growth advantages in 2D materials.

4. Conclusions

In summary, we have demonstrated one-pot CVD synthesis of 2D WS₂/MoS₂ heterostructures on polycrystalline Au foil. In particular, the vertical and lateral growth modes can be regulated by controlling the gas flow rate of H₂. WS₂/MoS₂ LHs are obtained without H₂ due to the good epitaxies between the two TMDs and the Au substrate. In contrast, WS₂/MoS₂ VHs are formed with 8–10 sccm H₂ introduced. This could result from the decreased surface absorption energy of W species on the pre-grown MoS₂ monolayer. Further increase in the H₂ flow rate not only leads to the formation of VHs but also causes etching of the as-grown MoS₂ edges. In addition, cross-contamination has been reduced via opposite directional transports of MoO₃/WO₃ and S vapors. Furthermore, we have shown the morphology evolution of the WS₂/MoS₂ VHs under different H₂ flow rates. This work provides a feasible method that could be extended towards the growth of other 2D TMDs-based heterostructures for high performance devices.

Supplementary Materials: The following supporting information can be downloaded at: <https://www.mdpi.com/article/10.3390/nano12101696/s1>. Figure S1. Typical optical microscopic images of monolayer MoS₂ and WS₂ domains grown on different substrates. (a) MoS₂ grown on SiO₂/Si at 750 °C for 20 min. (b) WS₂ grown on SiO₂/Si at 850 °C for 15 min. (c) MoS₂ grown on c-sapphire at 750 °C for 20 min. (d) WS₂ grown on c-sapphire at 850 °C for 15 min. Figure S2. Schematic diagrams of the growth of WS₂/MoS₂ LHs on Au foil and wet transfer from the Au foil onto a SiO₂/Si substrate. Figure S3. (a) Optical microscopic image of the CVD grown MoS₂/WS₂ LH on Au foil. (b) XPS spectrum of the heterojunction in (a). (c–f) XPS spectra of Au 4f (c), W 4f (d), Mo 3d (e) and S 2p (f) orbitals, respectively. Figure S4. Low-magnification optical microscopic images of the as-grown (a) WS₂/MoS₂ LHs and (b) WS₂/MoS₂ VHs on Au foils, respectively. Figure S5. Optical microscopic images of as-growth MoS₂/WS₂ VHs (a) growth on Au foils and as-transferred MoS₂/WS₂ VH (b) on SiO₂/Si, respectively. Figure S6. (a–d) Optical microscopic images of the synthesis LHs and VHs on SiO₂/Si and c-sapphire substrates depending on whether or not hydrogen is supplied. (e–h) AFM images of as-growth MoS₂/WS₂ LH and VH domains corresponding to (a–d). (i–l) AFM profiles along green dash line in (e–h), respectively.

Author Contributions: Synthesis, analysis, and writing—original draft preparation, Z.W.; Modification, W.X., Q.H. and B.L.; Synthesis, D.W. and H.G.; Transfer process, D.Q.; TEM, J.X.; Supervision and project administration, G.H. and W.Z. All authors have read and agreed to the published version of the manuscript.

Funding: This research was funded by the research fund of the University of Macau, Macau SAR (File No. MYRG2018-00079-IAPME, MYRG2019-00115-IAPME), the Science and Technology Development Fund, Macau SAR (File No. 081/2017/A2, 0059/2018/A2, 009/2017/AMJ), the Science, Technology, and Innovation Commission of Shenzhen Municipality (Grant No. JCYJ20200109105422876), the Educational Commission of the Guangdong Province project (Key program, Grant No. 2020ZDZX3041), and the Shenzhen Peacock Plan (Grant No. KQTD2016053112042971).

Institutional Review Board Statement: Not applicable.

Informed Consent Statement: Not applicable.

Data Availability Statement: Data are contained within the article and Supplementary Materials.

Conflicts of Interest: The authors declare no conflict of interest.

References

1. Butler, S.Z.; Hollen, S.M.; Cao, L.; Cui, Y.; Gupta, J.A.; Gutiérrez, H.R.; Heinz, T.F.; Hong, S.S.; Huang, J.; Ismach, A.F.; et al. Progress, Challenges, and Opportunities in Two-Dimensional Materials Beyond Graphene. *ACS Nano* **2013**, *7*, 2898–2926. [[CrossRef](#)] [[PubMed](#)]
2. Geim, A.K.; Grigorieva, I.V. Van der Waals heterostructures. *Nature* **2013**, *499*, 419–425. [[CrossRef](#)] [[PubMed](#)]
3. Liu, Y.; Huang, Y.; Duan, X. Van der Waals integration before and beyond two-dimensional materials. *Nature* **2019**, *567*, 323–333. [[CrossRef](#)] [[PubMed](#)]
4. Zhou, J.; Lin, J.; Huang, X.; Zhou, Y.; Chen, Y.; Xia, J.; Wang, H.; Xie, Y.; Yu, H.; Lei, J.; et al. A library of atomically thin metal chalcogenides. *Nature* **2018**, *556*, 355–359. [[CrossRef](#)] [[PubMed](#)]
5. Mak, K.F.; Lee, C.; Hone, J.; Shan, J.; Heinz, T.F. Atomically thin MoS₂: A new direct-gap semiconductor. *Phys. Rev. Lett.* **2010**, *105*, 136805. [[CrossRef](#)]
6. Lee, C.H.; Lee, G.H.; van der Zande, A.M.; Chen, W.; Li, Y.; Han, M.; Cui, X.; Arefe, G.; Nuckolls, C.; Heinz, T.F.; et al. Atomically thin p-n junctions with van der Waals heterointerfaces. *Nat. Nanotechnol.* **2014**, *9*, 676–681. [[CrossRef](#)]
7. Zhang, X.; Qiao, X.F.; Shi, W.; Wu, J.B.; Jiang, D.S.; Tan, P.H. Phonon and Raman scattering of two-dimensional transition metal dichalcogenides from monolayer, multilayer to bulk material. *Chem. Soc. Rev.* **2015**, *44*, 2757–2785. [[CrossRef](#)]
8. Jia, J.; Jeon, S.; Jeon, J.; Xu, J.; Song, Y.J.; Cho, J.H.; Lee, B.H.; Song, J.D.; Kim, H.J.; Hwang, E.; et al. Generalized Scheme for High Performing Photodetectors with a p-Type 2D Channel Layer and n-Type Nanoparticles. *Small* **2018**, *14*, 1703065. [[CrossRef](#)]
9. Chen, K.; Wan, X.; Wen, J.; Xie, W.; Kang, Z.; Zeng, X.; Chen, H.; Xu, J.-B. Electronic Properties of MoS₂-WS₂ Heterostructures Synthesized with Two-Step Lateral Epitaxial Strategy. *ACS Nano* **2015**, *9*, 9868–9876. [[CrossRef](#)]
10. Yu, W.J.; Liu, Y.; Zhou, H.; Yin, A.; Li, Z.; Huang, Y.; Duan, X. Highly efficient gate-tunable photocurrent generation in vertical heterostructures of layered materials. *Nat. Nanotechnol.* **2013**, *8*, 952–958. [[CrossRef](#)]
11. Chen, C.; Yang, Y.; Zhou, X.; Xu, W.; Cui, Q.; Lu, J.; Jing, H.; Tian, D.; Xu, C.; Zhai, T.; et al. Synthesis of Large-Area Uniform MoS₂-WS₂ Lateral Heterojunction Nanosheets for Photodetectors. *ACS Appl. Nano Mater.* **2021**, *4*, 5522–5530. [[CrossRef](#)]
12. Gong, Y.; Lin, J.; Wang, X.; Shi, G.; Lei, S.; Lin, Z.; Zou, X.; Ye, G.; Vajtai, R.; Yakobson, B.I.; et al. Vertical and in-plane heterostructures from WS₂/MoS₂ monolayers. *Nat. Mater.* **2014**, *13*, 1135–1142. [[CrossRef](#)] [[PubMed](#)]
13. Shi, J.; Tong, R.; Zhou, X.; Gong, Y.; Zhang, Z.; Ji, Q.; Zhang, Y.; Fang, Q.; Gu, L.; Wang, X.; et al. Temperature-Mediated Selective Growth of MoS₂/WS₂ and WS₂/MoS₂ Vertical Stacks on Au Foils for Direct Photocatalytic Applications. *Adv. Mater.* **2016**, *28*, 10664–10672. [[CrossRef](#)] [[PubMed](#)]
14. Zhu, J.; Li, W.; Huang, R.; Ma, L.; Sun, H.; Choi, J.-H.; Zhang, L.; Cui, Y.; Zou, G. One-pot selective epitaxial growth of large WS₂/MoS₂ lateral and vertical heterostructures. *J. Am. Chem. Soc.* **2020**, *142*, 16276–16284. [[CrossRef](#)]
15. Zhang, X.; Huangfu, L.; Gu, Z.; Xiao, S.; Zhou, J.; Nan, H.; Gu, X.; Ostrikov, K. Controllable Epitaxial Growth of Large-Area MoS₂/WS₂ Vertical Heterostructures by Confined-Space Chemical Vapor Deposition. *Small* **2021**, *17*, 2007312. [[CrossRef](#)]
16. Shi, J.; Ma, D.; Han, G.-F.; Zhang, Y.; Ji, Q.; Gao, T.; Sun, J.; Song, X.; Li, C.; Zhang, Y. Controllable growth and transfer of monolayer MoS₂ on Au foils and its potential application in hydrogen evolution reaction. *ACS Nano* **2014**, *8*, 10196–10204. [[CrossRef](#)]
17. Dong, J.; Zhang, L.; Dai, X.; Ding, F. The epitaxy of 2D materials growth. *Nat. Commun.* **2020**, *11*, 1–8. [[CrossRef](#)]
18. Zhang, X.; Nan, H.; Xiao, S.; Wan, X.; Gu, X.; Du, A.; Ni, Z.; Ostrikov, K.K. Transition metal dichalcogenides bilayer single crystals by reverse-flow chemical vapor epitaxy. *Nat. Commun.* **2019**, *10*, 598. [[CrossRef](#)]
19. Jeon, J.; Jang, S.K.; Jeon, S.M.; Yoo, G.; Jang, Y.H.; Park, J.-H.; Lee, S. Layer-controlled CVD growth of large-area two-dimensional MoS₂ films. *Nanoscale* **2015**, *7*, 1688–1695. [[CrossRef](#)]
20. Li, H.; Zhang, Q.; Yap, C.C.R.; Tay, B.K.; Edwin, T.H.T.; Olivier, A.; Baillargeat, D. From Bulk to Monolayer MoS₂: Evolution of Raman Scattering. *Adv. Funct. Mater.* **2012**, *22*, 1385–1390. [[CrossRef](#)]
21. Dhakal, K.P.; Duong, D.L.; Lee, J.; Nam, H.; Kim, M.; Kan, M.; Lee, Y.H.; Kim, J. Confocal absorption spectral imaging of MoS₂: Optical transitions depending on the atomic thickness of intrinsic and chemically doped MoS₂. *Nanoscale* **2014**, *6*, 13028–13035. [[CrossRef](#)] [[PubMed](#)]
22. Susarla, S.; Manimunda, P.; Morais Jaques, Y.; Hachtel, J.A.; Idrobo, J.C.; Syed Amnulla, S.A.; Galvão, D.S.; Tiwary, C.S.; Ajayan, P.M. Deformation Mechanisms of Vertically Stacked WS₂/MoS₂ Heterostructures: The Role of Interfaces. *ACS Nano* **2018**, *12*, 4036–4044. [[CrossRef](#)] [[PubMed](#)]
23. Kośmider, K.; Fernández-Rossier, J. Electronic properties of the MoS₂-WS₂ heterojunction. *Phys. Rev. B* **2013**, *87*, 075451. [[CrossRef](#)]
24. Kibsgaard, J.; Chen, Z.; Reinecke, B.N.; Jaramillo, T.F. Engineering the surface structure of MoS₂ to preferentially expose active edge sites for electrocatalysis. *Nat. Mater.* **2012**, *11*, 963–969. [[CrossRef](#)]

-
25. Xu, W.; Jung, G.; Zhang, W.; Wee, A.; Warner, J. Atomic sharpness of jagged edges of chemical vapor deposition-grown WS₂ for electrocatalysis. *Mater. Today Nano* **2022**, *18*, 100183. [[CrossRef](#)]
 26. Li, X.; Li, X.; Zang, X.; Zhu, M.; He, Y.; Wang, K.; Xie, D.; Zhu, H. Role of hydrogen in the chemical vapor deposition growth of MoS₂ atomic layers. *Nanoscale* **2015**, *7*, 8398–8404. [[CrossRef](#)]